The Astrophysical Journal, 992:73 (7pp), 2025 October 10 https://doi.org/10.3847/1538-4357/ae0627

Stringent Constraints on the Nuclear Matter Equation of State from Heavy Nuclei and Neutron Star Properties with a Multi-iteration Bayesian Statistical Analysis

Xue-Ying Jing[1,2] and Jian-Min Dong[1,2]
[1] Institute of Modern Physics, Chinese Academy of Sciences, Lanzhou 730000, People's Republic of China; dongjm07@impcas.ac.cn
[2] School of Nuclear Science and Technology, University of Chinese Academy of Sciences, Beijing 100049, People's Republic of China
Received 2025 May 6; revised 2025 September 8; accepted 2025 September 9; published 2025 October 7

Abstract

The equation of state (EoS) of dense nuclear matter, particularly the symmetry energy that characterizes its isospin dependence, is of fundamental importance in neutron star (NS) physics and nuclear physics. Apart from the extensively used multimessenger astrophysics information, we introduce three new constraints to tighten the EoS at intermediate densities: (i) the absent direct Urca process in the $1.5\,M_{\odot}$ NS; (ii) the symmetry energy (coefficient) $a_{\rm sym}$ of ^{208}Pb; (iii) the strong linear correlation between the slope parameter L of symmetry energy $E_{\rm sym}(\rho)$ at saturation density ρ_0 and $E_{\rm sym}(\rho_0) - a_{\rm sym}$. These constraints turn out to be highly effective for symmetry energy. As an alternative strategy, we employ the Bayesian statistical method with a multi-iteration procedure to ensure that the resulting posterior probability distribution is free of the initial prior distribution as far as possible. The most probable result of symmetry energy exhibits a soft behavior up to $\sim 2.5\rho_0$, and then it rises rapidly as the density increases. On the one hand, our results allow one to explore a series of topics in NS physics. For instance, the radius and tidal deformability for a $1.4\,M_{\odot}$ NS are $R_{1.4} = 12.46^{+0.22}_{-0.80}$ km and $\Lambda_{1.4} = 478^{+90}_{-183}$. The vast majority of NSs are unlikely to contain deconfined quark matter in their cores. On the other hand, almost all the widely used nuclear many-body approaches fail to reproduce such a trend of symmetry energy, and hence our results serve as an important calibration for nuclear force and nuclear many-body approaches.

Unified Astronomy Thesaurus concepts: Neutron stars (1108); Neutron star cores (1107); Pulsars (1306)

1. Introduction

The equation of state (EoS) of neutron star (NS) matter governed by quantum chromodynamics is a fundamental cornerstone in understanding the structure, composition, evolution, gravitational wave radiation, and lots of intriguing phenomena of NSs. Precise knowledge about the EoS is of enormous significance and has far-reaching applications in NS physics and nuclear physics. The EoS of zero-temperature asymmetric nuclear matter is expressed as an expansion of the energy per nucleon in terms of the isospin asymmetry β, given by I. Bombaci & U. Lombardo (1991) $E(\rho, \beta) \approx E_0(\rho) + E_{\rm sym}(\rho)\beta^2$, with the isospin asymmetry $\beta = (\rho_{\rm n} - \rho_{\rm p})/\rho$ and total nucleon density $\rho = \rho_{\rm n} + \rho_{\rm p}$. $\rho_{\rm n}(\rho_{\rm p})$ is the neutron (proton) number density. $E_0(\rho)$ denotes the energy per particle in symmetric nuclear matter. The symmetry energy (coefficient) $E_{\rm sym}(\rho)$, as an isospin-dependent component of the EoS, remains one of the most uncertain aspects, especially at high densities. Significant discrepancies persist among the predictions of hundreds of theoretical models (B. Sun et al. 2024). Yet, due to its importance, the density-dependent behavior of the symmetry energy has drawn great interest in both astrophysics (J. M. Lattimer & M. Prakash 2004; B. K. Sharma & S. Pal 2009; F. J. Fattoyev et al. 2013) and nuclear physics (P. Danielewicz et al. 2002; V. Baran et al. 2005; A. Steiner et al. 2005; B. A. Li et al. 2008; J. M. Dong et al. 2011).

Over the past two decades, a variety of terrestrial experiments have placed effective constraints on the EoS around the saturation density ($\rho_0 \approx 0.16\,{\rm fm}^{-3}$). These constraints arise from measurements about the properties of heavy atomic nuclei, such as giant and pygmy dipole resonance energies (S. Shlomo et al. 2006; J. Piekarewicz 2010; J. M. Lattimer 2023), neutron skin thickness in doubly magic nuclei (B. Alex Brown 2000; M. Centelles et al. 2009; S. Abrahamyan et al. 2012; E. Friedman 2012; Z. Zhang & L. W. Chen 2013), electric dipole polarizability (J. M. Lattimer 2023), excitation energies to isobaric analog states (P. Danielewicz & J. Lee 2014), charge radii of mirror nuclei (N. Wang & T. Li 2013; S. Gautam et al. 2024), nuclear mass, and decay energy (M. Liu et al. 2010; J. M. Dong et al. 2018). These observables provide valuable insights into the symmetry energy around or below the saturation density.

However, at suprasaturation densities, the behavior of the EoS or symmetry energy becomes increasingly uncertain and remains controversial. This ambiguity highlights the fundamental challenge of extending our understanding of the EoS to regimes relevant to NSs. To constrain it requires other strategies. Terrestrial heavy-ion collision experiments (M. B. Tsang et al. 2009; Y. X. Zhang et al. 2020; A. Venneti et al. 2024) serve as an important approach, whereas there is still no consensus among theoretical approaches (B. A. Li et al. 2008). Recently, many astrophysical observations of NSs provide crucial constraints on the nuclear matter EoS at high density, including the X-ray observations of quiescent and bursting NSs (A. W. Steiner et al. 2010), NS mass–radius (A. Li et al. 2017; N. B. Zhang et al. 2018), and gravitational waves from compact binary mergers (F. J. Fattoyev et al. 2014; N. B. Zhang & B. A. Li 2019; M. Jacobi et al. 2023; A. Thete et al. 2023; K. X. Huang et al. 2024; B. A. Li et al. 2024; B. K. Pradhan et al. 2024), potentially fast radio bursts (A. Moroianu et al. 2023; Z. Pan et al. 2023), and pulsar glitch

(P. Liu et al. 2024; O. H. Wilson & W. C. Ho 2024). Up to now, although significant progress has been achieved, the symmetry energy at high density remains highly uncertain.

In this work, we employ a Bayesian statistical method to infer the nuclear matter EoS. Previous studies have commonly utilized NS observables such as mass–radius and tidal deformability to constrain the high-density behavior of EoS (J. Zhou et al. 2023). We retain these observations, such as the data obtained from NS Interior Composition Explorer (K. C. Gendreau et al. 2016) and the LIGO-Virgo gravitational wave detectors (F. Özel & P. Freire 2016), as the underlying constraint in our analysis. To further constrain the EoS much more tightly, we additionally incorporate three new and valid constraints into our multi-iteration Bayesian framework, including the information of NS cooling (the DUrca process should not occur in typical NSs with masses below $1.5\,M_{\odot}$) and of measured atomic nuclear properties.

This work is organized as follows. Section 2 outlines the theoretical framework, including the basic aspects of EoS, the Bayesian statistical method, and the adopted constraints—in particular the new constraints we introduced. Section 3 presents the results and discussions. Finally, Section 4 provides a brief summary.

2. Theoretical Methods

2.1. EoS and NS Matter

The NS interior is assumed to be composed of neutrons, protons, and leptons (electrons and muons), without exotic degrees of freedom. We mainly focus on the dense matter at intermediate densities less than 3 times the saturation density, in which the exotic matter is unlikely to appear.

The EoS of asymmetric nuclear matter can be decomposed into two parts: the EoS for symmetric matter $E_0(\rho)$ and symmetry energy $E_{\rm sym}(\rho)$, expanded as

$$E_0(\rho) = E_0(\rho_0) + \frac{K_0}{2}\left(\frac{\rho-\rho_0}{3\rho_0}\right)^2 + \frac{J_0}{6}\left(\frac{\rho-\rho_0}{3\rho_0}\right)^3, \quad (1)$$

$$E_{\rm sym}(\rho) = E_{\rm sym}(\rho_0) + L\left(\frac{\rho-\rho_0}{3\rho_0}\right) + \frac{K_{\rm sym}}{2}\left(\frac{\rho-\rho_0}{3\rho_0}\right)^2 + \frac{J_{\rm sym}}{6}\left(\frac{\rho-\rho_0}{3\rho_0}\right)^3. \quad (2)$$

The Taylor expansion of the symmetry energy around saturation density provides a practical framework for describing the density dependence of the symmetry energy, although it exhibits systematic deviations in high-density regions. Currently, there exists no unified expression for this density-dependent behavior of the symmetry energy. Therefore, we employ a Taylor expansion to high order in Equation (2) to ensure its validity at intermediate densities less than $3\rho_0$ as far as possible, as done in W. J. Xie & B. A. Li (2019).

The EoS of symmetric matter relies on the incompressibility K_0 and skewness parameter J_0. The slope parameter L, curvature parameter $K_{\rm sym}$, and skewness parameter $J_{\rm sym}$ characterize the density-dependent behavior of the symmetry energy.

The energy density of the β-stable matter in the NS core is given by $\epsilon(\rho,\beta) = \rho E(\rho,\beta) + \rho m_n + \epsilon_l(\rho,\beta)$, where m_n and ϵ_l denote the nucleon rest mass and energy density of leptons, respectively. The charge neutrality $\rho_{\rm p} = \rho_{\rm e} + \rho_\mu$ and β-equilibrium $\mu_{\rm n} - \mu_{\rm p} = \mu_{\rm e} = \mu_\mu = 4\beta E_{\rm sym}(\rho)$ govern the composition of NS matter. The pressure of this NS matter is given by $P(\rho,\beta) = \rho^2 d[\epsilon(\rho,\beta)/\rho]/d\rho$.

The Baym–Pethick–Sutherland EoS is applied for the crust (G. Baym et al. 1971). With an EoS, the NS structure is built by solving the Tolman–Oppenheimer–Volkoff equation. In this work, we infer the parameters in Equations (1) and (2) in turn with the help of the observed information related to NS structure in combination with some properties of atomic nuclei.

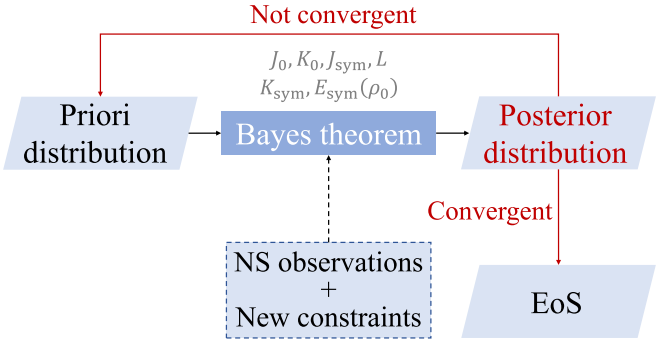

Figure 1. Flowchart of the parameter estimation based on a multi-iteration Bayesian statistical method. The multi-iteration procedure is performed, aiming at eliminating the dependence of the posterior probability distribution on the initial sampling. After the convergence is achieved, the ultimate EoS is obtained.

2.2. Multi-iteration Bayesian Statistical Method

The Bayesian statistical method provides a strategy to compute the posterior probability distribution of model parameters within Bayes theorem expressed as

$$P(M_i|D) = \frac{P(D|M_i)P(M_i)}{\sum_j P(D|M_j)P(M_j)}. \quad (3)$$

M_i denotes a specific theoretical model and $P(M_i)$ represents the prior probability distribution of theoretical parameters. D corresponds to observational or experimental data, and $P(D|M_i)$ is the likelihood function. The posterior probability distribution, $P(M_i|D)$, reflects the updated information of the theoretical parameters after incorporating the constraint conditions.

The prior distribution of the parameters is sampled using the Metropolis–Hastings algorithm within the Markov Chain Monte Carlo (MCMC) method, which is well suited for exploring complex, multidimensional probability distributions. Given the lack of prior knowledge of the parameter distributions, we adopt a uniform prior for the first sampling and then obtain the posterior probability distribution within the Bayes theorem. However, this result relies on the initial prior distribution. To eliminate such a dependency as much as possible, we use the obtained posterior probability distribution as a new prior distribution for the next iteration until the result converges. That is, we perform a multi-iterative scheme to achieve a convergent result, with the flowchart shown in Figure 1. To ensure that the obtained posterior probability distribution is reliable while also considering computational resources, we employ an MCMC sampling procedure consisting of 4 million steps. After discarding the burn-in phase, the posterior probability distribution for each individual parameter is obtained by integrating over the remaining parameters.

Table 1
Astronomical Observations of Pulsars, Including Maximum Mass, Mass–Radii, and Tidal Deformation, Used to Constrain the EoS of Dense Matter in Numerous Existing Studies and Our Present Work

Mass ($M_\odot$)	Tidal Deformability Λ	Source
1.4	190^{+390}_{-120} (90%)	GW170817 (1)
Mass($M_\odot$)	**Radius (km)**	**Source**
$1.44^{+0.15}_{-0.14}$	$13.02^{+1.24}_{-1.06}$ (68%)	PSR J0030+0451 (2)
$1.37^{+0.17}_{-0.17}$	$13.11^{+1.3}_{-1.3}$ (68%)	PSR J0030+0451 (3)
$1.42^{+0.04}_{-0.04}$	$11.36^{+0.95}_{-0.63}$ (68%)	PSR J0437−4715 (4)

References. (1) B. P. Abbott et al. (2018); (2) M. C. Miller et al. (2019); (3) S. Vinciguerra et al. (2024); (4) D. Choudhury et al. (2024).

The ranges of the prior distribution parameters in this work are guided by both microscopic nuclear many-body calculations and representative empirical constraints from nuclear experimental data. The incompressibility of symmetric matter, K_0, is determined through measurements of isoscalar giant monopole of heavy nuclei, with a typical value of $K_0 = 240 \pm 20$ MeV (S. Shlomo et al. 2006; J. Piekarewicz 2010). Using excitation energies to isobaric analog states, the symmetry energy $E_{\rm sym}(\rho_0)$ at saturation density is derived to be 30.2–33.7 MeV (P. Danielewicz & J. Lee 2014). A comprehensive review combining terrestrial experiments, neutron matter calculations, and astrophysical observations analyses reports an average value of $L = 58.7 \pm 28.1$ MeV (M. Oertel et al. 2017). Based on this, we set the prior range of the slope to $30\,{\rm MeV} \leqslant L \leqslant 90\,{\rm MeV}$. The skewness parameter of the symmetric matter and the curvature parameter of symmetry energy is poorly constrained within the range of $-800 \leqslant J_0 \leqslant 400$ MeV and $-400 \leqslant K_{\rm sym} \leqslant 100$ MeV, respectively (N. B. Zhang et al. 2017). The skewness parameters of the symmetry energy are taken as $-200 \leqslant J_{\rm sym} \leqslant 800$ MeV (I. Tews et al. 2017; N. B. Zhang et al. 2017). These higher-order terms are adopted in the same manner as in W. J. Xie & B. A. Li (2020).

2.3. Likelihood Function and the Constraint Selection

The likelihood function plays a central role in parameter estimation. By comparing the peak values of the posterior probabilities obtained from different likelihood functions, we can quantitatively evaluate how well the theoretical model fits the observational and experimental data. The details of the astronomical multimessenger observation data used here are summarized in Table 1, including the mass–radius and the tidal deformability. Massive works have been carried out to infer the EoS based on these constraints, thanks to the continuous progress of astronomical observations. We stress that, different from these studies, three additional constraints are introduced as follows:

Constraint 1: [DUrca]. The DUrca process (β-decay of neutron and its inverse reaction, $n \to p + e^- + \overline{\nu}_e$, $p + e^- \to n + \nu_e$), leading to a rapid cooling of NS, occurs just when the proton fraction is sufficiently high to ensure the momentum conservation. This fraction depends completely on the density-dependent symmetry energy (J. Boguta 1981; J. M. Lattimer et al. 1991). The average value of the slow pulsars (i.e., the small spin period pulsars and NSs with high-mass companions, which are likely to be near their birth masses) is 1.5 $M_\odot$ (F. Özel & P. Freire 2016). The fact that the vast majority of NS cooling observations can be well explained by the minimal cooling paradigm (D. Page et al. 2006) without fast neutrino emission means the DUrca process cannot occur in NSs with a mass of 1.5 $M_\odot$, and the threshold for the onset of the DUrca process should be evidently larger than 1.5 $M_\odot$. On the other hand, NS cooling simulations (D. Blaschke et al. 2004; T. Klähn et al. 2006) and population synthesis models of NSs (S. Popov et al. 2006) suggest that the DUrca process should not occur in typical NSs with masses below 1.5 $M_\odot$. In addition, various studies have proposed different threshold masses for the onset of DUrca processes: 1.6–1.8 $M_\odot$ (E. F. Brown & A. Cumming 2009; M. V. Beznogov & D. G. Yakovlev 2015; E. F. Brown et al. 2018; S. Beloin et al. 2019). Therefore, the absence of the DUrca process in the 1.5 $M_\odot$ NS is a rather conservative conclusion, which is employed as a constraint for the density-dependent behavior of the symmetry energy.

Constraint 2: [a_{sym}]. The symmetry energy (coefficient) $a_{\rm sym} = 23.7 \pm 0.4$ MeV of ^{208}Pb, as an important isovector indicator, has been extracted from experimental nuclear masses (J. M. Dong et al. 2018) where the charge-symmetry-breaking effects of strong nuclear force are taken into account. This result serves as an important constraint on the density-dependent symmetry energy around the saturation density. The symmetry energy term $E_{\rm sym}(A)$ of a spherical nucleus such as ^{208}Pb can be calculated by

$$E_{\rm sym}(A) = a_{\rm sym} I^2 A = \int \rho(r) E_{\rm sym}(\rho) \beta^2(r) 4\pi r^2 dr, \quad (4)$$

where $I = (N - Z)/A$ is isospin asymmetry of the nucleus. N, Z, and $A = N + Z$ are the neutron, proton, and mass numbers, respectively. We focus solely on the results for ^{208}Pb, with [$a_{\rm sym}$] specifically referring to the symmetry energy coefficient of ^{208}Pb. In practice, it represents a combination of the volume symmetry parameter and the surface symmetry parameter (M. Centelles et al. 2009). $\rho(r)$ is the nucleon density distribution, determined well by the widely used Skyrme–Hartree–Fock method with the SLy4 interaction.

Constraint 3: [$L - a_{sym}$]. J. M. Dong et al. (2015) achieved a linear correlation between the slope parameter L and the difference $E_{\rm sym}(\rho_0) - a_{\rm sym}$:

$$L = (9.682 \pm 0.285)(E_{\rm sym}(\rho_0) - a_{\rm sym}) - (42.694 \pm 3.441), \quad (5)$$

with a high correlation coefficient of 0.984. As the $a_{\rm sym}$ (symmetry energy coefficient of ^{208}Pb) is equal to the symmetry energy $E_{\rm sym}(\rho_0)$ of infinite nuclear matter at a reference density ρ_A (M. Centelles et al. 2009), this correlation can be derived in terms of $J - a_{\rm sym} = J - E_{\rm sym}(\rho_A) = E_{\rm sym}(\rho_0) - [E_{\rm sym}(\rho_0) + L(\rho_A - \rho_0)/3\rho_0 + ...] = -L(\rho_A - \rho_0)/3\rho_0 + ...$. The $E_{\rm sym}(\rho_0) - a_{\rm sym}$ actually characterizes the surface symmetry energy of the atomic nucleus. Although the theoretical predictions on L and $E_{\rm sym}(\rho_0)$ are diverse, such a linear correlation is robust and is confirmed in the realm of widely different nuclear functionals. The neutron skin thickness $\Delta R_{\rm np}$ of heavy nuclei also exhibits a tight linear correlation with the slope parameter L. However, recent experimental determinations of the parity-violating asymmetry in ^{48}Ca and ^{208}Pb at

Jefferson Lab displays incompatible results in constraining symmetry energy (D. Adhikari et al. 2021, 2022), so they are not of much help at present.

These conditions allow us to constrain the EoS further in combination with extensively used multimessenger astrophysics information. The posterior probability distribution of the theoretical parameters is obtained by applying the likelihood function of

$$P(D|M_i) = P_{\rm filter} \times P_{\rm maxmass} \times P_{\rm radius} \times P_{\rm tidal} \times P_{\rm Urca} \times P_{\rm a_{sym}} \times P_{\rm La_{sym}}. \quad (6)$$

Here $P_{\rm filter}$ represents three essential physical conditions that must be satisfied in the NS model: (1) the pressure at the crust–core boundary layer must be positive $P_\tau > 0$; (2) the EoS must satisfy the thermodynamic stability condition $\partial P/\partial\epsilon \geqslant 0$; (3) causality (sound speed is lower than the light speed $v_s/c \leqslant 1$) is satisfied at all densities. $P_{\rm maxmass}$ ensures that the EoS is sufficiently stiff to support the observed maximum mass of NSs. The mass–radius observational data of PSR J0751+1807 and other massive NSs are not employed in this study as the high-density regime ($\rho > 3\rho_0$) inside these massive NSs may potentially contain exotic matter. We focus on the EoS of normal nuclear matter at densities $\rho \leqslant 3\rho_0$. Table 1 presents two mass–radius measurements of PSR J0030 +1807 obtained through independent methodologies. Since neither method demonstrates clear superiority, we incorporate both measurements in our analysis, as done in W. J. Xie & B. A. Li (2020). $P_{\rm radius}$, $P_{\rm tidal}$, and $P_{\rm a_{sym}}$ are expressed with Gaussian likelihood functions:

$$P_{\rm radius},\ P_{\rm tidal},\ P_{\rm a_{sym}} \propto \exp\left[-\frac{(X_{\rm model} - X_{\rm obs})^2}{2\sigma_i^2}\right]. \quad (7)$$

$P_{\rm La_{sym}}$ measures the correlation strength between L and the $E_{\rm sym}(\rho_0) - a_{\rm sym}$:

$$P_{\rm La_{sym}} \propto \exp\left[-\frac{(L - \langle L\rangle)^2}{2\sigma^2}\right], \quad (8)$$

where L is the value of the slope parameter sampled from the model and $\langle L\rangle$ is the corresponding value derived from Equation (5).

3. Result and Discussion

Although the combination of gravitational wave signals and mass–radius measurements provides valuable insights into the EoS, it remains insufficient to place very tight constraints on the EoS. The uncertainties in these measured data are still considerable. Therefore, apart from these observational data, we further introduce three constraints as mentioned above. The posterior probability distributions of the six EoS expansion parameters (J_0, K_0, $J_{\rm sym}$, $K_{\rm sym}$, L, and $E_{\rm sym}(\rho_0)$) in Equations (1) and (2) are computed using the Bayesian statistical method. Figure 2 displays the 68% credible regions of the converged posterior probability distributions for each parameter. To demonstrate the sensitivity of the EoS to these three constraints we mentioned above, three sets of likelihood function configurations are shown in each panel, labeled as $[a_{\rm sym}]$, $[a_{\rm sym}]$ + [DUrca], and $[a_{\rm sym}]$ + [DUrca] + $[L - a_{\rm sym}]$. These curves allow for a comparative evaluation of the impact

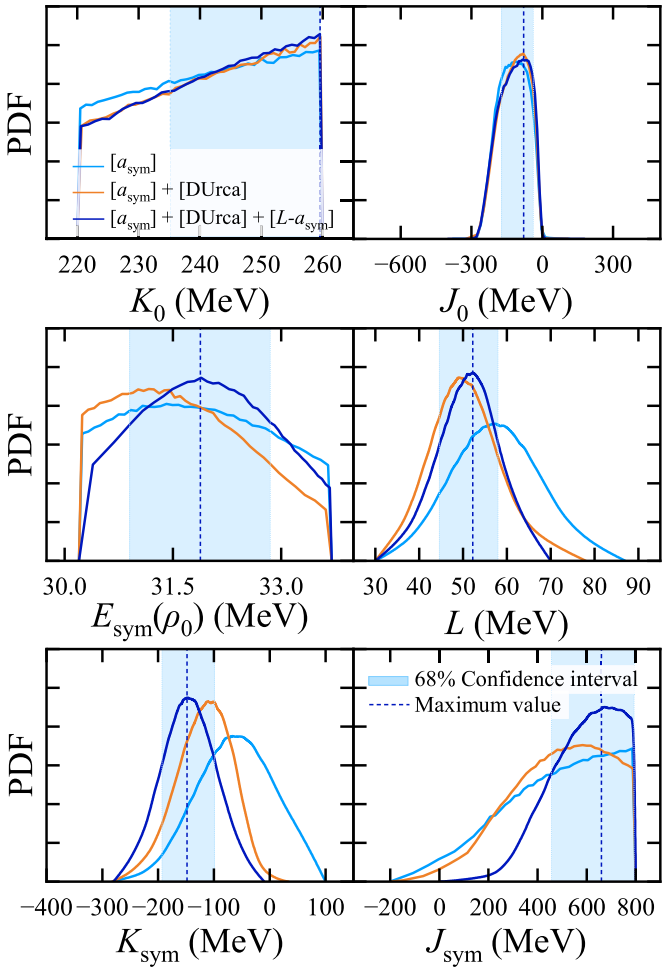

Figure 2. Posterior probability distribution functions of the six EoS parameters: K_0, J_0, $E_{\rm sym}(\rho_0)$, L, $K_{\rm sym}$, and $J_{\rm sym}$. The sky-blue curve corresponds the constraint $[a_{\rm sym}]$, the orange curve represents $[a_{\rm sym}]$ + [DUrca], and the blue curve shows the result with the full constraint set $[a_{\rm sym}]$ + [DUrca] + $[L - a_{\rm sym}]$. The shaded regions denote the 68% confidence intervals, and the red dashed lines indicate the most probable values.

of each constraint. The vertical red dashed lines indicate the most probable value of each parameter.

Figure 2 clearly shows the peaks of J_0, $E_{\rm sym}(\rho_0)$, L, and $K_{\rm sym}$, while K_0 remains approximately uniformly distributed. The inferred value of J_0 is $-78.9^{+40.9}_{-93.6}$ MeV, consistent with that obtained in W. J. Xie & B. A. Li (2020). Both our K_0 and J_0 values are systematically larger than those obtained from X-ray observations of quiescent and bursting NSs (A. W. Steiner et al. 2010). The EoS of symmetric matter, i.e., $E_0(\rho)$ as a function of density ρ, appears to be largely unaffected by these three constraints and does not show substantial improvement compared with previous studies. This finding suggests that constraining symmetric nuclear matter, particularly the incompressibility K_0, may require additional constraints from other approaches.

The three new constraints we introduce have a major impact on the four parameters of the symmetry energy. The DUrca condition, inferred from NS cooling observations, is tightly correlated with the proton fraction in the stellar core. Therefore, it imposes a constraint on the proton fraction or isospin asymmetry β, and hence it is able to constrain the $J_{\rm sym}$, $K_{\rm sym}$, L, and $E_{\rm sym}(\rho_0)$ effectively as the symmetry energy determines the proton fraction. The $[L - a_{\rm sym}]$ constraint

Table 2
The Obtained Most Probable Values and 68% Confidence Intervals for the Six Parameters of the EoS and for E_0 along with $E_{\rm sym}$ at $2\rho_0$ and $3\rho_0$

Parameters	Value (MeV)	Parameters	Value (MeV)
K_0	$260.0^{+0.0}_{-24.9}$	J_0	$-78.9^{+40.9}_{-93.6}$
$E_{\rm sym}(\rho_0)$	$31.9^{+0.9}_{-0.9}$	L	$52.2^{+5.7}_{-7.6}$
$K_{\rm sym}$	$-148.1^{+44.8}_{-49.1}$	$J_{\rm sym}$	$659.9^{+140.1}_{-203.4}$
$E_0(2\rho_0)$	$-1.8^{+0.1}_{-2.1}$	$E_{\rm sym}(2\rho_0)$	$45.1^{+6.3}_{-7.8}$
$E_0(3\rho_0)$	$38.8^{+1.1}_{-11.0}$	$E_{\rm sym}(3\rho_0)$	$66.4^{+22.2}_{-25.9}$

strongly constrains the density dependence of the symmetry energy near the saturation density, leading to more precise determinations of both symmetry energy J and the slope parameter L. This results in a more concentrated confidence range for J and L. As shown in Figure 2, the confidence ranges of higher-order coefficients are also reduced because the two adjacent parameters, such as J and L, $K_{\rm sym}$, and $J_{\rm sym}$, exhibit anticorrelations (W. J. Xie & B. A. Li 2020). Therefore, the higher-order terms are indirectly affected, and $K_{\rm sym}$ and $J_{\rm sym}$ consequently develop more pronounced peaks.

The posterior distribution of the theoretical parameters enables us to achieve the basic properties of nuclear matter and of NSs. Employing all the constraints we list, the final most probable values, along with their 68% confidence intervals, are summarized in Table 2. We conclude that $L = 52.2^{+5.7}_{-7.6}$ MeV and $K_{\rm sym} = -148.1^{+44.8}_{-49.1}$ MeV. Intriguingly, these two parameters, as two very key parameters of the EoS, exhibit the steepest peaks as well as narrow bands. The prior range for the lower-order parameter $E_{\rm sym}(\rho_0)$ is intrinsically narrow, resulting in a posterior result of $E_{\rm sym}(\rho_0) = 31.9^{+0.9}_{-0.9}$ MeV. However, the higher-order parameter $J_{\rm sym}$ has the broadest range in both prior and posterior distributions, so the constrained confidence interval remains larger.

Subsequently, we calculate the EoS of symmetric matter $E_0(\rho)$ and the symmetry energy $E_{\rm sym}(\rho)$ with the six EoS expansion parameters listed in Table 2 based on Equations (1) and (2). The density dependence of these two quantities is exhibited in Figure 3, with 68% confidence intervals under different constraints. The calculations in the blue region take into account all the constraints in Equation (6). The dashed line is calculated from the most probable values of the six parameters. A comparison of the constraint ranges in the upper panel reveals that the three additional constraints exert no significant influence on the behavior of $E_0(\rho)$, consistent with but more intuitive than that presented in Figure 2. The most substantial constraint on $E_0(\rho)$ still arises from the structure information on NSs.

We are more interested in the density-dependent symmetry energy. As shown in the lower panel of Figure 3, the progressive application of the three constraints leads to the systematic exclusion of the very stiff symmetry energy at high densities. This trend also demonstrates the effectiveness of these constraints in narrowing the uncertainty in the symmetry energy, also in agreement with but more intuitive than the results presented in Figure 2. Importantly, the uncertainty in the symmetry energy at high density is reduced visibly, and thus the obtained results should be very useful in both astronomy and nuclear physics. The symmetry energy is soft around the saturation density, but it becomes increasingly stiff

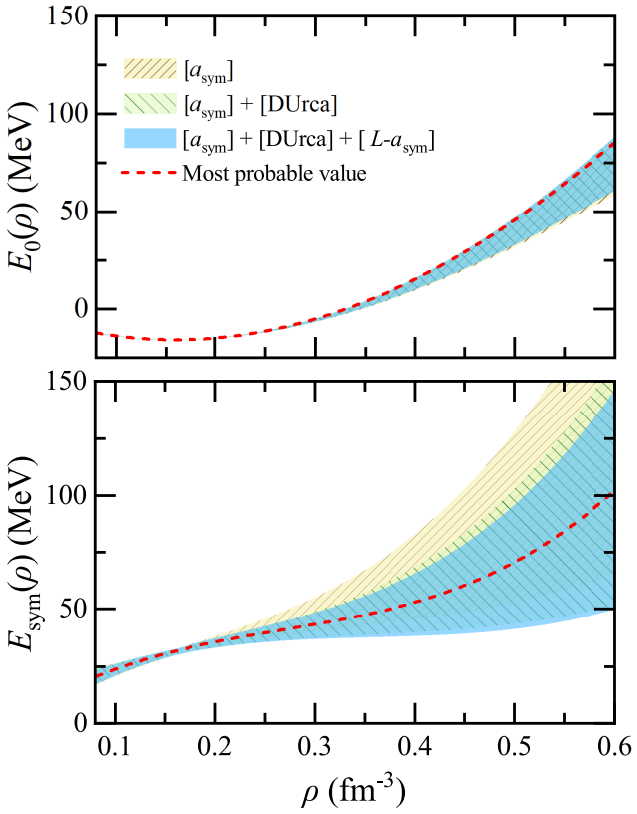

Figure 3. (Upper panel) EoS of symmetric nuclear matter (i.e., energy per particle vs. density) and (lower panel) the density-dependent symmetry energy. The yellow, green, and blue shaded areas are based on $[a_{\rm sym}]$, $[a_{\rm sym}]$ + [DUrca], and $[a_{\rm sym}]$ + [DUrca] + $[L - a_{\rm sym}]$ constraints, respectively. The dashed line shows the most probable value obtained from the full set of constraints, which are given by $E_0(\rho) = -0.968 - 189.691\rho + 621.332\rho^2 - 118.951\rho^3$ and $E_{\rm sym}(\rho) = 2.174 + 288.015\rho - 798.814\rho^2 + 994.481\rho^3$ for $\rho > \rho_0/2$.

as the density increases. It rises rapidly with density ρ after $\sim$2.5 ρ_0, resulting in the slope being larger than the stiffest symmetry energy predicted by various models. This behavior also leads to higher pressure in the high-density region of NSs. The most probable EoS in our analysis predicts a maximum NS mass of 2.4 $M_\odot$.

To further grasp the high-density behavior of the EoS at certain densities of interest, Table 2 provides the computed values of $E_0(\rho)$ and $E_{\rm sym}(\rho)$ at $2\rho_0$ and $3\rho_0$, respectively. W. J. Xie & B. A. Li (2019) inferred the high-density symmetry energy from representative $R_{1.4}$ data, obtaining a lower central value of $E_{\rm sym}(2\rho_0) = 39.2^{+12.1}_{-8.2}$ MeV. Both N. B. Zhang & B. A. Li (2019) and Y. Li et al. (2021) used NS radius, maximum mass, tidal deformability, and causality condition to constrain the symmetry energy, yielding $E_{\rm sym}(2\rho_0) = 46.9 \pm 10.1$ and $E_{\rm sym}(2\rho_0) = 34.5^{+20.5}_{-2.3}$ MeV, respectively. Our result of $E_{\rm sym}(2\rho_0) = 45.1^{+6.3}_{-7.8}$ MeV is basically consistent with these recent studies and with the fiducial value of 47 MeV reported in W. J. Xie & B. A. Li (2020), but it exhibits a smaller uncertainty.

We predict the radius of a 1.4 $M_\odot$ NS to be $12.46^{+0.22}_{-0.80}$ ($12.46^{+0.31}_{-2.83}$) km at 68% (95%) confidence level, with a corresponding tidal deformability of $\Lambda_{1.4} = 478^{+90}_{-183}$. In addition, we obtain a moment of inertia of $I_{1.4} = 1.576^{+0.050}_{-0.190} \times 10^{38}$ kg m^2 for a 1.4 $M_\odot$ NS and $I_{1.338} = 1.460^{+0.055}_{-0.165} \times 10^{38}$ kg m^2 for a

$1.338\,M_\odot$ NS. Using combined nuclear experimental and astrophysical observational constraints, Y. Lim & J. W. Holt (2022) reported $I_{1.338} = 1.425^{+0.074}_{-0.146} \times 10^{38}\,\mathrm{kg\,m^2}$ for PSR J0737–3039A with mass of $1.338\,M_\odot$, consistent with our result.

The onset of hyperons in dense matter substantially softens the EoS, and hence the calculated NS maximum mass is not compatible with measured values, known as the hyperon puzzle in NSs. It has been suggested that a symmetry energy that is relatively soft at low densities but stiffens at high densities provides a probable explanation for the hyperon puzzle (J. T. Ye et al. 2024). The symmetry energy we derived exactly captures this trend, suggesting that this longstanding puzzle is likely to be resolved. Our calculation shows that the stellar mass increases rapidly with rising central density. For a massive NS with the mass of $2.01\,M_\odot$, its central density is $0.53\,\mathrm{fm}^{-3}$ ($\simeq 3.3\rho_0$), which is lower than that predicted by vast majority of EoS models. Recent studies based on geometric percolation of the baryon radius suggest a reasonable critical density for the appearance of deconfined quark at densities in the range of $(4–7)\rho_0$ (G. Baym et al. 2018). Therefore, it is unlikely that deconfined quark matter exists in the interiors of most NSs.

Finally, we assess the validity of various nuclear many-body methods since their calculated EoSs present strong model dependence. We compare our results with the EoS obtained with various methods, including Skyrme–Hartree–Fock, relativistic mean-field, Brueckner–Hartree–Fock, relativistic Brueckner–Hartree–Fock (RBHF), and variational method with frequently used interactions, as shown in Figure 4. The trend that the symmetry energy is soft at low density but becomes increasingly stiff at high density cannot be well reproduced by any method listed in Figure 4, although many models (such as SKA, SK272, SK255, SKI2, SKM*, SKMP, IMP2, LNS1, LNS5, HFB17, IUFSU, RBHF-Bonn B, and RBHF-Bonn C) can satisfy the constraint on $E_0(\rho)$. The symmetry energy provided by just the Akmal–Pandharipande–Ravenha (APR) EoS exhibits a strong consistency with our results below $\sim 2.5\,\rho_0$. Anyway, the density-dependent symmetry energy we obtained here serves as an important calibration for a reliable construction of nuclear energy density functionals.

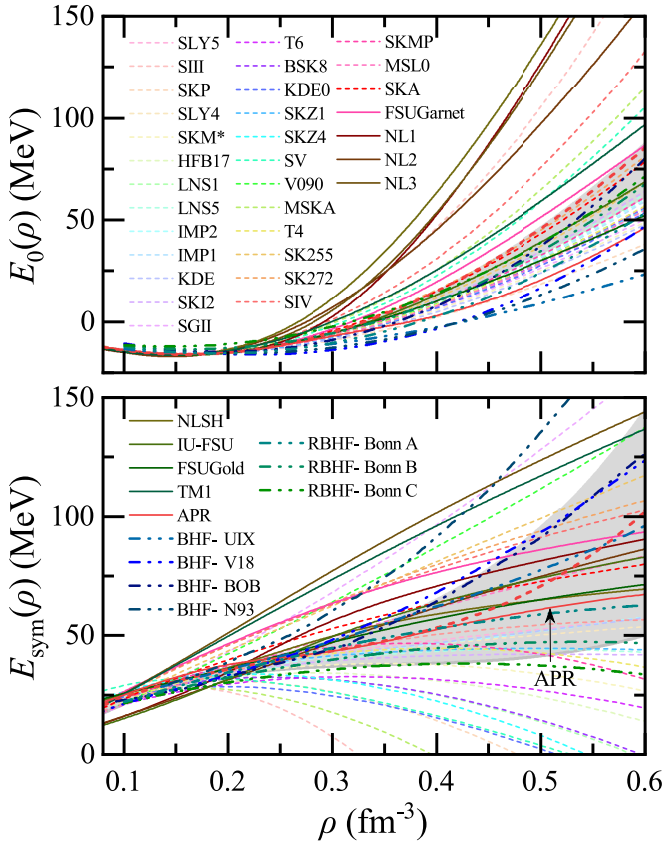

Figure 4. Our constrained EoS compared with the theoretically calculated ones with various nuclear many-body approaches such as the APR EoS (red solid line; A. Akmal et al. 1998), the relativistic mean-field method (the other solid lines), the Skyrme–Hartree–Fock method (short dashed lines), the Brueckner–Hartree–Fock (blue double-dotted–dashed lines; Z. H. Li & H. J. Schulze 2008), and the relativistic Brueckner–Hartree–Fock (green double-dotted–dashed lines; H. Tong et al. 2022). The long red dashed line is the most probable value of $E_0(\rho)$ and $E_{\rm sym}(\rho)$ we obtained.

4. Summary

We constrain the EoS of nuclear matter, in particular, the density-dependent symmetry energy, by combining multi-faceted astronomical observations of NSs and properties of heavy atomic nuclei based on the Bayesian statistical method. Different from previous studies, three new and valid constraints are taken into account: the absent DUrca process in $1.5\,M_\odot$ canonical NS, symmetry energy (coefficient) $a_{\rm sym} = 23.7 \pm 0.4\,\mathrm{MeV}$ of ^{208}Pb, and linear correlation between L and $E_{\rm sym}(\rho_0) - a_{\rm sym}$. To eliminate the dependence of the posterior probability distribution on the prior distribution, we introduce a multi-iterative convergence strategy as an important improvement in methodology. The result shows that the inclusion of these constraints gives significant peak in the parameters, particularly for slope L and curvature $K_{\rm sym}$ of symmetry energy, which are predicted to be $L = 52.2^{+5.7}_{-7.6}\,\mathrm{MeV}$ and $K_{\rm sym} = -148.1^{+44.8}_{-49.1}\,\mathrm{MeV}$, respectively. The symmetry energy at saturation density is tightly constrained to be $E_{\rm sym}(\rho_0) = 31.9^{+0.9}_{-0.9}\,\mathrm{MeV}$. Although the skewness $J_{\rm sym}$ has a large uncertainty due to its larger prior range, it shows a noticeable sensitivity to these constraints. In a word, the uncertainty in the symmetry energy at high density is reduced substantially. The symmetry energy at certain density points of interest is finally determined to be $E_{\rm sym}(2\rho_0) = 45.1^{+6.3}_{-7.8}\,\mathrm{MeV}$ and $E_{\rm sym}(3\rho_0) = 66.4^{+22.2}_{-25.9}\,\mathrm{MeV}$. In addition, our model yields the values of the radius, moment of inertia, and tidal deformability of a $1.4\,M_\odot$ NS as $R_{1.4} = 12.46^{+0.22}_{-0.80}\,\mathrm{km}$, $I_{1.4} = 1.576^{+0.050}_{-0.190} \times 10^{38}\,\mathrm{kg\,m^2}$, and $\Lambda_{1.4} = 478^{+90}_{-183}$, respectively. Finally, we provide a fitted form of the most probable EoS to facilitate future applications.

The most probable result of symmetry energy exhibits a soft behavior around the saturation density, but it rises rapidly as the density increases after $\sim 2.5\rho_0$. This trend is expected to solve the longstanding hyperon puzzle, which requires further study in detail. The central density of a $2.01M_\odot$ massive NS is just about $3.3\rho_0$, still below the critical density for deconfined quark emergence. Thus most NSs do not have deconfined quarks in their interiors. In addition, our results can be used to assess the different EoS models or interactions. Although many interactions such as SKA, SK272, SK255, SKI2, SKM*, SKMP, IMP2, LNS1, LNS5, HFB17, IUFSU, RBHF-Bonn B, and RBHF-Bonn C are able to reproduce our constrained EoS of symmetry matter, almost all the interactions widely used at current fail to reproduce the trend of the symmetry energy (only the APR EoS yields the symmetry energy that is

consistent with our results below $2.5\rho_0$). In other words, our result rules out the vast majority of EoS models. Therefore, our study not only provides critical insight into the dense matter properties and allows one to explore a series of properties and phenomena of NSs related to nuclear matter such as structure, gravitational wave radiation, glitches, free-body precession, quasiperiodic oscillation, spin evolution, magnetic inclination angle evolution, hydrogen-poor superluminous supernovae, and gamma burst (millisecond magnetars as the candidate central engines), but it also serves as an important calibration for nucleon–nucleon interaction and building of nuclear many-body approaches.

Acknowledgments

We thank Prof. Wenjie Xie for the helpful discussions. This work is supported by the National Natural Science Foundation of China under grants No. 12222511, by the Chinese Academy of Sciences Project for Young Scientists in Basic Research YSBR-088, and by the Strategic Priority Research Program of Chinese Academy of Sciences, grant No. XDB34000000.

ORCID iDs

Jian-Min Dong https://orcid.org/0000-0001-9625-7860

References

Abbott, B. P., Abbott, R., Abbott, T. D., et al. 2018, PhRvL, 121, 161101
Abrahamyan, S., Ahmed, Z., Albataineh, H., et al. 2012, PhRvL, 108, 112502
Adhikari, D., Albataineh, H., Androic, D., et al. 2021, PhRvL, 126, 172502
Adhikari, D., Albataineh, H., Androic, D., et al. 2022, PhRvL, 129, 042501
Akmal, A., Pandharipande, V. R., & Ravenhall, D. G. 1998, PhRvC, 58, 1804
Alex Brown, B. 2000, PhRvL, 85, 5296
Baran, V., Colonna, M., Greco, V., & Di Toro, M. 2005, PhR, 410, 335
Baym, G., Hatsuda, T., Kojo, T., et al. 2018, RPPh, 81, 056902
Baym, G., Pethick, C., & Sutherland, P. G. 1971, ApJ, 170, 299
Beloin, S., Han, S., Steiner, A. W., & Odbadrakh, K. 2019, PhRvC, 100, 055801
Beznogov, M. V., & Yakovlev, D. G. 2015, MNRAS, 452, 540
Blaschke, D., Grigorian, H., & Voskresensky, D. N. 2004, A&A, 424, 979
Boguta, J. 1981, PhLB, 106, 255
Bombaci, I., & Lombardo, U. 1991, PhRvC, 44, 1892
Brown, E. F., & Cumming, A. 2009, ApJ, 698, 1020
Brown, E. F., Cumming, A., Fattoyev, F. J., et al. 2018, PhRvL, 120, 182701
Centelles, M., Roca-Maza, X., Viñas, X., & Warda, M. 2009, PhRvL, 102, 122502
Choudhury, D., Salmi, T., Vinciguerra, S., et al. 2024, ApJL, 971, L20
Danielewicz, P., Lacey, R., & Lynch, W. G. 2002, Sci, 298, 1592
Danielewicz, P., & Lee, J. 2014, NuPhA, 922, 1
Dong, J. M., Wang, L. J., Zuo, W., & Gu, J. Z. 2018, PhRvC, 97, 034318
Dong, J. M., Zuo, W., & Gu, J. Z. 2015, PhRvC, 91, 034315
Dong, J. M., Zuo, W., & Scheid, W. 2011, PhRvL, 107, 012501
Fattoyev, F. J., Carvajal, J., Newton, W. G., & Li, B. A. 2013, PhRvC, 87, 015806
Fattoyev, F. J., Newton, W. G., & Li, B. A. 2014, EPJA, 50, 45
Friedman, E. 2012, NuPhA, 896, 46
Gautam, S., Venneti, A., Banik, S., & Agrawal, B. 2024, NuPhA, 1043, 122832
Gendreau, K. C., Arzoumanian, Z., Adkins, P. W., et al. 2016, Proc. SPIE, 9905, 99051H
Huang, K. X., Shen, H., Hu, J. N., & Zhang, Y. 2024, PhRvC, 109, 045804
Jacobi, M., Guercilena, F. M., Huth, S., et al. 2023, MNRAS, 527, 8812
Klähn, T., Blaschke, D., Typel, S., et al. 2006, PhRvC, 74, 035802
Lattimer, J. M. 2023, Parti, 6, 30
Lattimer, J. M., Pethick, C. J., Prakash, M., & Haensel, P. 1991, PhRvL, 66, 2701
Lattimer, J. M., & Prakash, M. 2004, Sci, 304, 536
Li, A., Zhu, Z. Y., & Zhou, X. 2017, ApJ, 844, 41
Li, B. A., Chen, L. W., & Ko, C. M. 2008, PhR, 464, 113
Li, B. A., Grundler, X., Xie, W. J., & Zhang, N. B. 2024, PhRvD, 110, 103040
Li, Y., Chen, H., Wen, D., & Zhang, J. 2021, EPJA, 57, 31
Li, Z. H., & Schulze, H. J. 2008, PhRvC, 78, 028801
Lim, Y., & Holt, J. W. 2022, Galax, 10, 99
Liu, M., Wang, N., Li, Z. X., & Zhang, F. S. 2010, PhRvC, 82, 064306
Liu, P., Yuan, J. P., Ge, M. Y., et al. 2024, MNRAS, 533, 4274
Miller, M. C., Lamb, F. K., Dittmann, A. J., et al. 2019, ApJL, 887, L24
Moroianu, A., Wen, L. Q., James, C. W., et al. 2023, NatAs, 7, 579
Özel, F., & Freire, P. 2016, ARA&A, 54, 401
Oertel, M., Hempel, M., Klähn, T., & Typel, S. 2017, RvMP, 89, 015007
Page, D., Geppert, U., & Weber, F. 2006, NuPhA, 777, 497
Pan, Z., Yang, H., & Yagi, K. 2023, PhRvD, 108, 063014
Piekarewicz, J. 2010, JPhG, 37, 064038
Popov, S., Grigorian, H., Turolla, R., & Blaschke, D. 2006, A&A, 448, 327
Pradhan, B. K., Ghosh, T., Pathak, D., & Chatterjee, D. 2024, ApJ, 966, 79
Sharma, B. K., & Pal, S. 2009, PhLB, 682, 23
Shlomo, S., Kolomietz, V. M., & Colò, G. 2006, EPJA, 30, 23
Steiner, A., Prakash, M., Lattimer, J., & Ellis, P. 2005, PhR, 411, 325
Steiner, A. W., Lattimer, J. M., & Brown, E. F. 2010, ApJ, 722, 33
Sun, B., Bhattiprolu, S., & Lattimer, J. M. 2024, PhRvC, 109, 055801
Tews, I., Lattimer, J. M., Ohnishi, A., & Kolomeitsev, E. E. 2017, ApJ, 848, 105
Thete, A., Banerjee, K., & Malik, T. 2023, PhRvD, 108, 063028
Tong, H., Wang, C. C., & Wang, S. B. 2022, ApJ, 930, 137
Tsang, M. B., Zhang, Y. X., Danielewicz, P., et al. 2009, PhRvL, 102, 122701
Venneti, A., Gautam, S., Banik, S., & Agrawal, B. 2024, PhLB, 854, 138756
Vinciguerra, S., Salmi, T., Watts, A. L., et al. 2024, ApJL, 961, 62
Wang, N., & Li, T. 2013, PhRvC, 88, 011301
Wilson, O. H., & Ho, W. C. 2024, PhRvD, 109, 083006
Xie, W. J., & Li, B. A. 2019, ApJ, 883, 174
Xie, W. J., & Li, B. A. 2020, ApJ, 899, 4
Ye, J. T., Wang, R., Wang, S. P., & Chen, L. W. 2025, ApJ, 985, 238
Zhang, N. B., Cai, B. J., Li, B. A., Newton, W. G., & Xu, J. 2017, NuScT, 28, 181
Zhang, N. B., & Li, B. A. 2019, EPJA, 55, 39
Zhang, N. B., Li, B. A., & Xu, J. 2018, ApJ, 859, 90
Zhang, Y. X., Liu, M., Xia, C. J., Li, Z. X., & Biswal, S. K. 2020, PhRvC, 101, 034303
Zhang, Z., & Chen, L. W. 2013, PhLB, 726, 234
Zhou, J., Xu, J., & Papakonstantinou, P. 2023, PhRvC, 107, 055803